DIRECT NUMERICAL SIMULATIONS OF AIRFOIL CASCADES FOR THE IMPROVEMENT OF TURBULENCE MODELS THROUGH DATABASE GENERATION

M. Rasquin[1] - J.-F. Thomas[1] - T. Toulorge[1] -
P. Bechlars[2] - M. Franke[2] - K. Hillewaert[1,3]

[1]Cenaero, Belgium,
{michel.rasquin}{jean-francois.thomas}{thomas.toulorge}{koen.hillewaert}@cenaero.be
[2]MTU Aero Engines AG, Germany, {patrick.bechlars}{matthias.franke}@mtu.de
[3]University of Liège, Belgium, koen.hillewaert@uliege.be

ABSTRACT

Direct Numerical Simulations (DNS) of a typical LPT airfoil cascade at a Reynolds number of 120,000 have been carried out with the high-order compressible flow solver Argo developed at Cenaero. The objective of these simulations is to generate highly-refined comprehensive databases in a systematic and reproducible manner, which allows the reconstruction of all terms of the Favre-averaged Navier-Stokes, Reynolds stress, and dissipation equations. These databases can then be exploited to improve the prediction of lower-fidelity approaches such as RANS turbulence models, which allow for an extensive exploration of the design space thanks to their low computational cost. This paper presents a systematic approach for generating such databases. Particular points of interest are the reproducibility of the boundary conditions (*e.g.* , injection of freestream turbulence) and the completeness of the databases. Comparison between the numerical and experimental results will also be presented as a validation of the numerical setup.

KEYWORDS

DIRECT NUMERICAL SIMULATION, DISCONTINUOUS GALERKIN METHOD, AIRFOIL CASCADE, TURBULENCE INJECTION, ADVANCED STATISTICS FOR TURBULENCE MODELING

NOMENCLATURE

c_{ax}	axial chord	Ω_{ij}	rotation rate tensor
L_p	pitch	τ_{ij}	viscous stress tensor
ρ	density	δ_{ij}	Kronecker symbol
p	pressure	ν	kinematic viscosity
T	temperature	ω_i	i-th vorticity component
u_i	i-th velocity component	DGM	Discontinuous Galerkin Method
k	kinetic energy	DHIT	Decay of Homogeneous Isotropic Turbulence
$\mathcal{S}_{ij}$	strain rate tensor	LPT	Low Pressure Turbine

INTRODUCTION

Turbomachinery design currently relies on the Reynolds Averaged Navier-Stokes (RANS) turbulence modeling approach (*e.g.* see Wilcox et al. (1998), Menter et al. (2003), Spalart

(2010)), which allows for an extensive exploration of the design space. However, RANS models suffer from lower reliability for complex geometries and flow configurations which feature laminar to turbulent flow transition and flow separation to name a few (Hunt and Savill (2005)). One way to address the deficiencies of current statistical models of turbulence consists in taking a more direct and holistic approach to the direct derivation of such models. The present work aims at generating highly-refined comprehensive DNS databases in a systematic and reproducible manner which allows the reconstruction of all terms of the Favre-averaged Navier-Stokes, the Reynolds stress and the dissipation equations. The resulting databases can then be used not only for the calibration of existing turbulence models, but also the development of new models, through for instance machine learning (Duraisamy et al. (2019)).

A key ingredient for the generation of high quality databases in an industrial context is the advent of unstructured high order accurate methods, such as the Discontinuous Galerkin method (DGM, Cockburn et al. (2012)). These methods have paved the way for high-resolution adaptive Direct Numerical Simulation (DNS) and Large Eddy Simulation (LES) of complex geometries characteristic of turbomachinery. Although a direct application of scale-resolving simulations including boundary layers to full components is currently out of reach, detailed simulations of blade sections and cascades at very high resolution can already be performed relatively routinely. In that context, direct numerical simulations of the midsection of a typical low pressure turbine (LPT) airfoil cascade have been carried out at a Reynolds number of 120,000 with the high-order compressible DGM flow solver Argo developed at Cenaero.

In the next sections, the workflow used to setup these DNS will be presented, including the injection of freestream turbulence based on an homogeneous isotropic turbulence precursor simulation. Comparison between the numerical and experimental results in terms of isentropic Mach number distribution on the blade and total pressure losses in the wake will also be presented as a validation of the numerical setup. The TKE and dissipation fields near the trailing edge on the suction side of the blade, which are part of the resulting high-fidelity databases, will finally be briefly presented along with their residual budget.

NUMERICAL APPROACH

Argo is based on a high-order Discontinuous Galerkin Method (DGM) which discretizes the compressible Navier-Stokes equations (*e.g.* Carton de Wiart et al. (2014), Carton de Wiart et al. (2015)). This code can deal with any arbitrary unstructured hybrid curved meshes where elements of different topology and accuracy can be accommodated, as well as localised refinement in the zones of interest. In this work, an implicit time integrator based on Jacobian-free Newton-GMRES preconditioned with block-Jacobi is used. High-order methods including DGM are characterized by highly compact stencil which lends themselves to efficient parallel implementations. This computational efficiency can lead to important reductions in restitution time with respect to conventional codes (see Vincent et al. (2016)).

FREE-STREAM TURBULENCE INJECTION

Turbulence Injection Methods

A broad range of methods has been proposed in the literature to inject a turbulent flow with prescribed properties through an inlet boundary condition. These approaches can be roughly classified into two categories: *synthetic methods* and *recycling methods*.

Synthetic turbulence methods generate fluctuations using analytical expressions (Dhamankar et al. (2018)). Although many extensions are proposed to satisfy basic relations in turbulent

flows, which mimic flow structures and provide the necessary temporal and spatial correlations, the fluctuations generated by these methods are not fully compliant with real turbulent flows (Keating and Piomelli (2006)). Thus, they usually require extending the computational domain upstream so that a realistic turbulent flow can develop, which incurs a larger computational cost.

Recycling turbulence methods (Wu (2017)) use an auxiliary computation to generate a turbulent flow, that is imposed as boundary data at the inlet of the main simulation. These methods include *precursor* or *co-simulation* approaches, which provide high-quality inlet data since only very minor deviations from the actual configuration (e.g. Taylor's frozen turbulence hypothesis) are used to generate them. Moreover, no or minor transition is to be expected due to numerical issues. For these reasons, recycling approaches seem better suited to generate reference data for model development. This quality comes however at the expense of some loss of flexibility (*e.g.* simulation setup, domain size), which can only be obtained through synthetic methods.

Precursor Simulation

The free-stream turbulence injection procedure used in this work consists in performing a *precursor* simulation yielding a realisation of a turbulent free-stream flow with zero mean velocity. The resulting velocity fluctuations u'' are then combined with the mean flow $\widetilde{u}_{in}$ at the inlet of the main simulation. The technique is based on two hypotheses. The Taylor *frozen turbulence* hypothesis uses $u'' \ll \widetilde{u}_{in}$ to neglect the non-linear interaction between turbulence and mean advection. Moreover, the turbulence time scales are supposed to be much larger than the convection time scales. Therefore the turbulent fluctuations can be considered as merely convected by the mean flow. The second hypothesis is that the flow is spatially homogeneous, even in the direction of the flow. Under both hypotheses, it is sufficient to use a precursor solution, frozen at a given time corresponding to the desired turbulent kinetic energy (TKE) and length scale. The inlet plane is then swept through this solution at the main inlet velocity $\widetilde{u}_{in}$. Adding the velocity fluctuations interpolated on the inlet plane to the mean velocity gives the full turbulent inlet velocity $\widetilde{u}_{in} + u''$. From this full turbulent inlet velocity and the imposed total pressure and total temperature, the conservative variables are computed and imposed at the interpolation points of the main inlet. This Dirichlet boundary condition will finally be propagated to the main domain by the computation of the fluxes through the inlet plane and a Riemann solver. It should be noted that using the perturbed velocity allows to maintain the total temperature as imposed. However due to the higher dissipation the total pressure is destroyed more rapidly in the domain and this effect has to be compensated to respect the mean value from the measurements near the blade, especially for large velocity fluctuations.

Decay of Homogeneous Isotropic Turbulence

The precursor simulation considered in this work computes the canonical case of the decay of homogeneous isotropic turbulence (DHIT) in a triply periodic cube (Pope (2000)). The precursor simulation is setup in order to obtain statistical properties in its final frozen solution that match the level of turbulence intensity through the level of TKE and the correlation length specified for the inlet of the main simulation. Although the flow around the blade section is compressible, it is assumed that the inlet turbulent fluctuations are incompressible. Thus, an initial incompressible velocity field with zero mean is imposed in the precursor simulation following the method proposed by Rogallo (1981). Its energy content follows a spectrum defined by Passot and Pouquet (1987). The amplitude and the spectral width of this spectrum control the initial TKE and the initial integral length (with respect to the precursor domain size). The
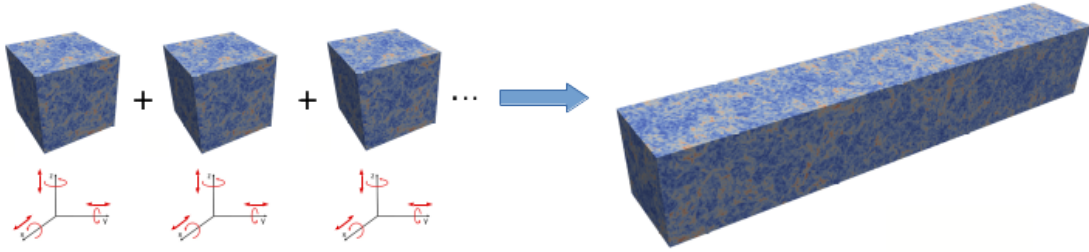
Figure 1: **Concatenation process applied to the frozen DHIT precursor solution**

initial total temperature and pressure are set to be uniform.

Implementation

In practice, several difficulties related to the computational cost of such a procedure arise. First, the precursor simulation becomes too costly if its spatial extent in the directions parallel to the boundary covers the whole inlet plane of the main simulation. The problem is overcome by performing a precursor simulation of limited size and using several copies of the precursor field in the pitchwise and/or spanwise directions. This solution may however introduce spurious spatial correlations in the inlet turbulent field.

Second, due to the limited (and common) extent in all directions of the precursor simulation, one would have a very high correlation in the streamwise direction, which is considered as much more detrimental than in the pitchwise and spanwise directions. This problem is addressed by a concatenation and blending technique inspired by Xiong et al. (2004) and Larsson (2009). Several realisations of the DHIT domain, obtained by random rotations and translation of the original DHIT solution, are concatenated in the streamwise direction to obtain a longer period in time, as illustrated in Figure 1. The resulting domain retains periodicity in spanwise and pitchwise directions, as well as in the streamwise direction along which its size has been multiplied. In this way, the main simulation can run for an indefinite duration by cycling in time through the concatenated precursor domain along its streamwise direction. However, a plain concatenation procedure would create discontinuities in the injected turbulent flow. Therefore, the concatenation is complemented with a blending technique that ensures a smooth turbulent solution over the whole streamwise extent. A final projection of the velocity field on a divergence-free space removes compressibility artifacts introduced by the blending.

In summary, this free-stream turbulence injection procedure consists of three steps: 1) Setup and execution of the precursor simulation, 2) duplication, transformation, concatenation and blending of the precursor solution field, and 3) setup and execution of the main simulation.

ADVANCED STATISTICS FOR RANS MODELLING

Notations

In what follows, Cartesian components are indicated with indices i, j or k. For instance, the velocity components are denoted as u_i. The derivatives of first and second order are respectively noted as

$$a_{,i} \hat{=} \frac{\partial a}{\partial x_i} \quad \text{and} \quad a_{,ij} \hat{=} \frac{\partial^2 a}{\partial x_i \partial x_j} \tag{1}$$

The Einstein notation is used throughout the text, entailing summation on repeated indices.

Consequently, the inner product of two vectors and the divergence of a vector are respectively noted as

$$a_i b_i \hat{=} \sum_{i=1}^{3} a_i b_i = \mathbf{a} \cdot \mathbf{b} \quad \text{and} \quad a_{i,i} \hat{=} \sum_{i=1}^{3} a_{i,i} = \nabla \cdot \mathbf{a} \tag{2}$$

The Reynolds average of a quantity q and its associated fluctuation result from the ensemble average

$$\overline{q}(x, y, z, t) = \frac{1}{N} \sum_{l=1}^{N} q_l(x, y, z, t) \tag{3}$$

$$q'(x, y, z, t) = q(x, y, z, t) - \overline{q}(x, y, z, t) \tag{4}$$

with the index l running on the N realisations of the flow field. For statistically stationary flows, l will correspond to a snapshot in a time series. The Favre average is based upon the density weighted ensemble average and the associated fluctuations

$$\widetilde{q} = \frac{\overline{\rho \, q}}{\overline{\rho}} \tag{5}$$

$$q''(x, y, z, t) = q(x, y, z, t) - \widetilde{q}(x, y, z, t) \tag{6}$$

Statistics for RANS Modeling

To improve RANS models, the statistical accumulation of all the terms deriving from three distinct equations are considered here, namely the Favre averaged Navier-Stokes, the Reynolds stress and the dissipation equations. The Favre averaged Navier-Stokes equations (not developed here) follows the formulation proposed by Knight (1997) whereas the Reynolds stress equation follows the formulation proposed by Gerolymos and Vallet (2001):

$$\mathcal{R}_{ij,t} + (\mathcal{R}_{ij}\widetilde{u}_k)_{,k} = P_{ij} + D_{ij} + \Phi_{ij} + \Phi'_{ij} - \epsilon_{ij} + K_{ij} \tag{7}$$

where

$$\mathcal{R}_{ij} = \overline{\rho u''_i u''_j} \qquad \qquad \text{Reynolds stress} \tag{8}$$

$$P_{ij} = -\mathcal{R}_{ik}\widetilde{u}_{j,k} - \mathcal{R}_{jk}\widetilde{u}_{i,k} \qquad \qquad \text{production term} \tag{9}$$

$$D^1_{ij} = -\left(\overline{\rho u''_i u''_j u''_k}\right)_{,k} \qquad \qquad \text{turbulent diffusion term} \tag{10}$$

$$D^2_{ij} = -\left(\overline{p'(u''_i \delta_{jk} + u''_j \delta_{ik})}\right)_{,k} \qquad \qquad \text{pressure diffusion term} \tag{11}$$

$$D^3_{ij} = \left(\overline{u''_i \tau'_{jk} + u''_j \tau'_{ik}}\right)_{,k} \qquad \qquad \text{viscous diffusion term} \tag{12}$$

$$\Phi_{ij} = \overline{p'(u''_{i,j} + u''_{j,i} - \frac{2}{3}u''_{k,k}\delta_{ij})} \qquad \qquad \text{pressure strain term} \tag{13}$$

$$\Phi'_{ij} = \frac{2}{3}\overline{p'u''_{k,k}\delta_{ij}} \qquad \qquad \text{pressure-dilatation term} \tag{14}$$

$$\epsilon_{ij} = \overline{\tau'_{jk}u''_{i,k} + \tau'_{ik}u''_{j,k}} \qquad \qquad \text{viscous dissipation term} \tag{15}$$

$$K_{ij} = -u''_i \left(\overline{p_{,j}} - \overline{\tau_{jk,k}}\right) - u''_j \left(\overline{p_{,i}} - \overline{\tau_{ik,k}}\right) \qquad \text{density fluctuation effects} \tag{16}$$

The equation for the TKE is found by computing the trace of all the terms in the Reynolds stress equations. These quantities are therefore not stored separately. More details about the

formulation for the Favre averaged Navier-Stokes and Reynolds stress equations used in this work are provided by Hillewaert and Rodi (2022).

The most complex equation is the one governing the kinetic energy dissipation ϵ. The compressible form of ϵ is divided into a solenoidal ϵ_s, a dilatation ϵ_d and finally an non-homogeneous part ϵ_i. Kreuzinger et al. (2006) state that the last two contributions are negligible for moderately compressible flows, and therefore these are not considered here. The solenoidal part of the dissipation is given by

$$\epsilon_s = \widetilde{\nu}\overline{\omega_i'\omega_i'} \tag{17}$$

and its evolution equation

$$\frac{D\epsilon_s}{Dt} = P_\epsilon^1 + P_\epsilon^2 + P_\epsilon^3 + P_\epsilon^4 + T_\epsilon + D_\epsilon - \Upsilon + F_\epsilon + T_\epsilon^C + B_\epsilon + \frac{\epsilon_s}{\widetilde{\nu}}\frac{D\nu}{Dt} \tag{18}$$

where

$$P_\epsilon^1 = 4\widetilde{\nu}\,\overline{\Omega_{ij}'u_{k,j}'}\,\overline{u_{i,k}} \qquad \text{1st turbulent production term} \tag{19}$$

$$P_\epsilon^2 = 4\widetilde{\nu}\,\overline{\Omega_{ij}'u_{i,k}'}\,\overline{u_{k,j}} \qquad \text{2nd turbulent production term} \tag{20}$$

$$P_\epsilon^3 = 4\widetilde{\nu}\,\overline{\Omega_{ij}'u_k'}\,\overline{u_{i,jk}} \qquad \text{production term by mean vorticity gradient} \tag{21}$$

$$P_\epsilon^4 = 4\widetilde{\nu}\,\overline{\Omega_{ij}'u_{i,k}'u_{k,j}'} \qquad \text{production term by vortex stretching} \tag{22}$$

$$T_\epsilon = 2\widetilde{\nu}\left(\overline{u_k'\Omega_{ij}'u_{i,j}'}\right)_{,k} \qquad \text{turbulent transport term} \tag{23}$$

$$T_\epsilon^C = -2\widetilde{\nu}\overline{\Omega_{ij}'u_{i,j}'u_{k,k}'} \qquad \text{the compressible turbulent transport term} \tag{24}$$

$$D_\epsilon = -4\widetilde{\nu}\,\overline{\left(v\Omega_{ij}'\tau_{ik,j}\right)_{,k}} \qquad \text{the viscous diffusion term} \tag{25}$$

$$\Upsilon = -4\widetilde{\nu}\,\overline{\left(v\Omega_{ij}'\right)_{,k}\tau_{ik,j}} \qquad \text{the viscous destruction term} \tag{26}$$

$$F_\epsilon = -4\widetilde{\nu}\,\overline{\Omega_{ij}'v_{,j}\tau_{ik,k}} \qquad \text{the viscous stress term} \tag{27}$$

$$B_\epsilon = 4\widetilde{\nu}\,\overline{\Omega_{ij}'\,p_{,i}v_{,j}} \qquad \text{the baroclinic term} \tag{28}$$

Statistics Acquisition

While direct averages such as $\overline{u_i}$ and baseline correlation such as the density velocity correlation $\overline{\rho u_i}$ are straightforward to compute, some care has to be taken when considering correlations between fluctuations, since they are supposed to be computed with respect to a converged average, according to Equations 4 and 6. Considering the Reynolds stress $\mathcal{R}_{ij} = \overline{\rho u_i''u_j''}$, the prior convergence of $\widetilde{u}_i$ is fortunately not necessary to approximate the evaluation of $\mathcal{R}_{ij}$. The most straightforward way to compute correlations of fluctuations, which also is the least sensitive to round-off error, is to accumulate simple baseline correlations from which correlations between fluctuations can be reconstructed only when needed, *e.g.* as a post-processing step when exporting the output data to disk. Considering again the Reynolds stress, $\mathcal{R}_{ij}$ can be computed from the expression

$$\mathcal{R}_{ij} = \overline{\rho u_i''u_j''} = \overline{\rho u_i u_j} - \overline{\rho}\widetilde{u}_i\widetilde{u}_j \tag{29}$$

Similarly, the triple velocity correlation $\overline{\rho u_i''u_j''u_k''}$ found in the turbulent diffusion term of the Reynolds stress equation in Equation 10 can be computed according to the combination

$$\overline{\rho u_i''u_j''u_k''} = \overline{\rho u_i u_j u_k} - \overline{\rho u_j u_k}\widetilde{u}_i - \overline{\rho u_k u_i}\widetilde{u}_j - \overline{\rho u_i u_j}\widetilde{u}_k + 2\overline{\rho}\widetilde{u}_i\widetilde{u}_j\widetilde{u}_k \tag{30}$$

Consequently, only direct averages and baseline correlations are accumulated throughout the computation and stored in checkpoints, whereas the actual correlations between fluctuations are computed via post-processing. As a result, the lists of averages and baseline correlations needed for reconstructing the data sets include about 200 terms.

If the flow possesses a homogeneous direction (*i.e.* spanwise direction for a bi-periodic air-foil cascade), the averaging procedure implemented in this work includes first a spatial average of 3D instantaneous quantities of interest over this direction before being accumulated in time. The result may then be stored on the associated periodic plane, which drastically reduces the IO bandwidth when saving a checkpoint, the disk storage, and the associated post-processing burden without implying any simplification (*i.e.* reduction of indices) of the resulting correlations.

AIRFOIL CASCADE

The considered geometry is the midsection profile of a typical LPT airfoil cascade. This LPT blade is a modern low-Reynolds profile which has been investigated intensively in the wind tunnel of the University of Armed Forces in Munich. Considering the indices 1 and 2 related to the inlet and outlet of the domain respectively, the operating point of this profile is defined by an isentropic Reynolds number $Re_{2th} = 120000$, an isentropic Mach number $M_{2th} \approx 0.6$, a total pressure $p_{t1} \approx 16000$ Pa, a total temperature $T_{t1} \approx 300$ K, a static pressure $p_2 \approx 12000$ Pa and an inflow angle $\beta_1 = 120°$.

Numerical setup

A second-order 2D curved mesh with structured elements in the boundary layer and unstructured elements in the passage is first generated using the open source mesh generator Gmsh (Geuzaine and Remacle (2009)) and then extruded in the spanwise direction, resulting in about 1.9M hexahedra. Computations are then carried out with the high-order DGM code Argo. Fourth-order (P4) Lagrange polynomials are used for the representation of the solution, corresponding to a fifth-order accurate simulation with about 236M degrees of freedom per equation. In the laminar region of the flow, the mesh resolution s^+/p and z^+/p on the blade surface (cell size in the streamwise and spanwise direction in wall units divided by the polynomial degree) is equal to respectively 4 and 3 upstream the separation of the boundary layer. Further downstream, s^+/p and z^+/p are both less than 3 in the separation region and around 6 in the turbulent region after the reattachment of the boundary layer. Note that the spanwise resolution is constant in the whole domain and isotropic in the separation and turbulent region of the blade. In the wall-normal direction, n^+ is less than 1 in the laminar and turbulent regions, and less than 0.5 in the separation region. The h/η_K ratio between an estimation of the mesh size and the Kolmogorov length scale near the trailing edge on the suction side of the blade is finally presented in Figure 2. The mesh size h is computed as the cubic root of the hexahedra volume divided by the polynomial degree and the Kolmogorov length scale as $\eta_K = \sqrt[4]{(\mu^3/\overline{\rho}^2)/(\tau'_{ij}S''_{ij})}$. The h/η_K ratio is less than 1 in most of the domain except after the reattachment in the turbulent region of the blade where it rises to 2 and in the close wake of the blade where a maximum value of 4 is computed.

An adiabatic no-slip wall boundary condition is applied to the blade profile whereas total conditions (p_{t1} and T_{t1}) are imposed at the inlet and static pressure p_2 at the outlet. Periodic boundary conditions are finally imposed in the spanwise and pitchwise directions.

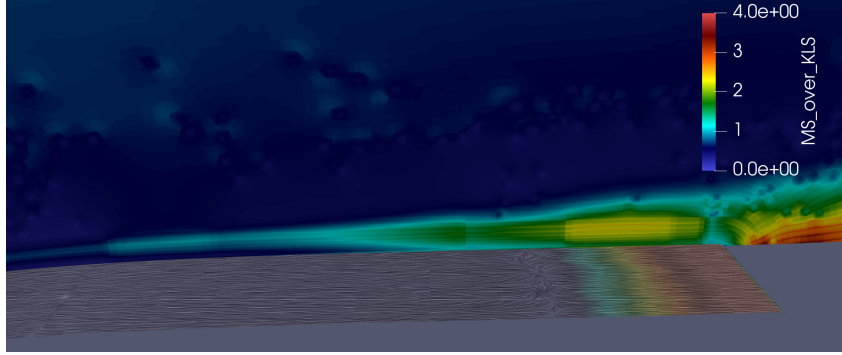The advanced statistics for the generation of high-fidelity databases were formerly vali-

Figure 2: **Mesh size to Kolmogorov length scale ratio near the trailing edge on the suction side of the blade**

dated with traditional benchmarks such as the channel flow test case and then collected over 17 convective time units (CTU) for the LPT blade; a CTU corresponds to a flow over the chord considering the inlet velocity. 2M core hours on 8192 cores of the in-house AMD EPYC super-computer Lucia hosted at Cenaero were used to compute these 17 CTU.

Precursor Simulation Setup

To limit the cost of the simulation, a span equal to 20% of the pitch is prescribed to the main simulation domain. Consequently, the size of the cubic domain of the precursor DHIT simulation (illustrated in the left part of Figure 1) is also set equal to this span length. In this way, the inlet surface of the main simulation domain can be covered in the pitchwise direction by five copies of the long blended DHIT turbulent box (illustrated in the right part of Figure 1). A span equal to 20% of the pitch corresponds to about 20% of the axial cord, which was checked to be wide enough to ensure an acceptable reduction of the correlation level of all velocity components to 10% at most in the close wake of the blade.

For the setup of the precursor DHIT simulation, experimental measurements of the TKE and the integral length scales upstream of the airfoil cascade in the wind tunnel were provided from hot-wire measurements. However, the experimental integral length scale, estimated through auto-correlations of velocity fluctuations and the Taylor hypothesis of frozen turbulence, corresponds to 86% of the axial chord and was therefore too large to be matched numerically due to limitations of the span length and the computational cost. The largest integral length scale allowed by the simulation was therefore about 10% of the experimental length scale. These smaller turbulent scales also lead to a higher dissipation of the TKE than desired, which had to be counterbalanced by the injection of a higher level of TKE at the inlet of the numerical domain to target the same level of TKE estimated at the streamwise location of the blade in the middle passage from three experimental measurements upstream the blade (marked as k_{ref} hereafter). Note that although some anisotropy in the velocity fluctuations was measured experimentally between the streamwise direction and the two other directions normal to the flow, the homogeneous isotropic turbulence assumption was deemed acceptable.

The TKE evolution in the precursor DHIT simulation is illustrated in Figure 3. Relying on the Taylor hypothesis, a correspondence can be established between the elapsed time of the DHIT simulation and the distance covered by the flow from the inlet of the main simulation domain to the streamwise location of the blade based on the convection velocity. The initial
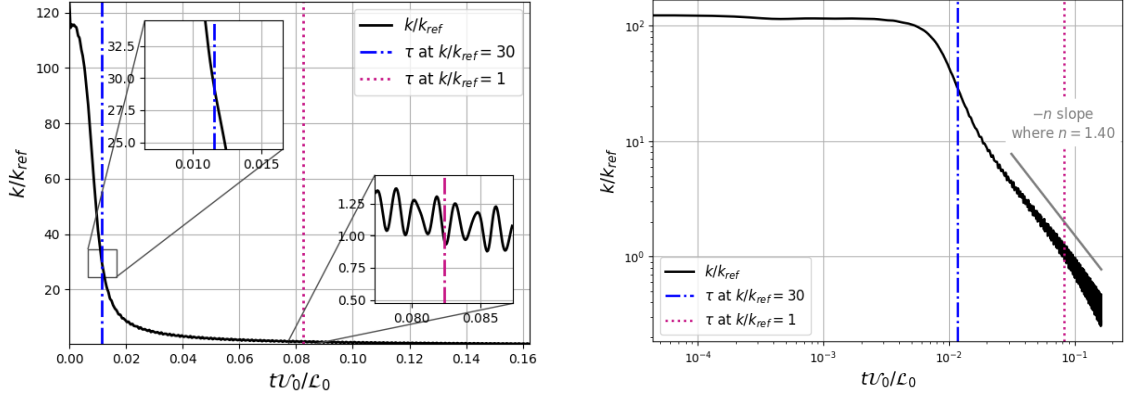
Figure 3: **Evolution of the TKE in the DHIT precursor simulation normalized by the estimated experimental TKE at the blade**
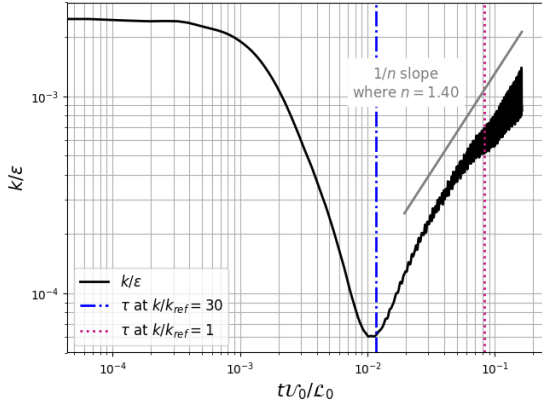

Figure 4: **Evolution of k/ϵ in the DHIT precursor simulation**
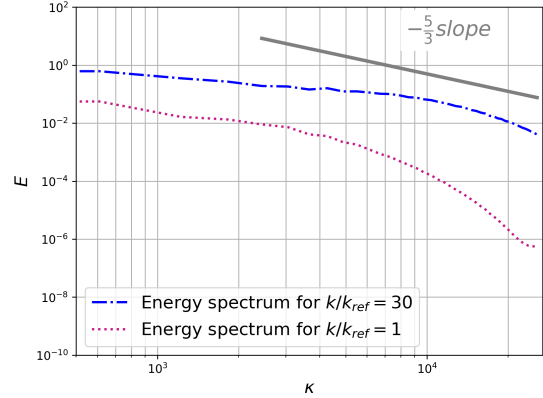

Figure 5: **Energy spectra of the DHIT precursor simulation**

TKE of the Passot-Pouquet spectrum is set to about $124\ k_{ref}$ in this precursor simulation. The magenta dotted line in Figure 3 corresponds to the target $k = k_{ref}$ at the blade. The blue dashed line corresponds to the selected state of the DHIT simulation ($k = 30\ k_{ref}$) which was frozen to generate the blended turbulent box illustrated in Figure 1 and injected later in the blade domain. Ideally, the time difference between the blue dashed line (frozen turbulence for the main simulation) and the magenta dotted line ($k = k_{ref}$) corresponds to the time required by turbulent structures injected at the inlet of the main simulation domain to reach the blade.

Afterwards, the canonical state of the frozen turbulence at $k = 30\ k_{ref}$ is assessed. As illustrated in the right log-log plot of Figure 3, the precursor simulation is characterized by a transient TKE plateau due to the non-physical character of the initial Passot-Pouquet spectrum. After the initial transient, the canonical TKE decay establishes with a decay exponent n ranging between 1.15 and 1.45 as discussed by Cocle et al. (2009) and Pope (2000). As shown in Figure 4 with the evolution of the TKE over the dissipation, the canonical decay of turbulence is also expected to start once k/ϵ has reached a minimum and follows a typical slope of $1/n$. In both figures, the selected frozen state of the DHIT simulation at $k = 30\ k_{ref}$ (blue dashed line) appears at the beginning of the canonical region of TKE decay. Finally, the energy spectra of
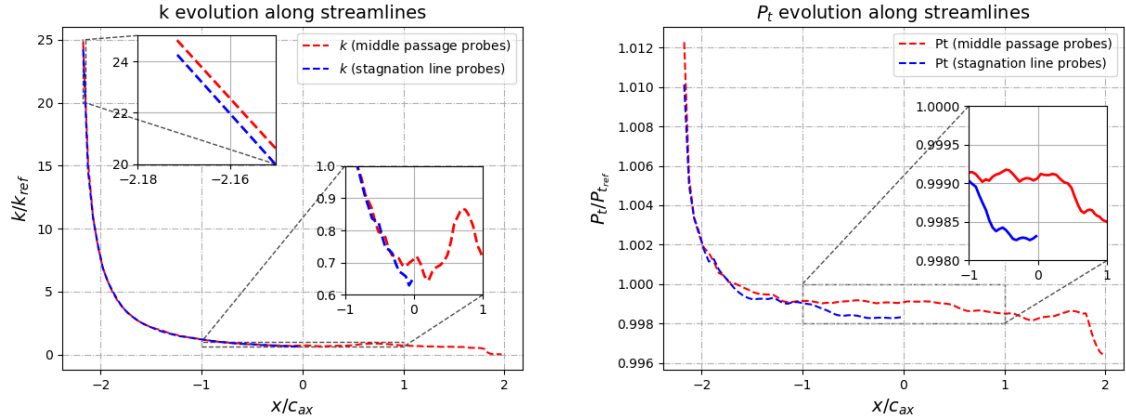
Figure 6: **Evolution of the TKE and total pressure in the blade domain**

the DHIT simulation at $k = 30 \, k_{ref}$ and $k = k_{ref}$ are plotted in Figure 5. Despite the strong decay of turbulence due to a smaller integral length scale, the expected energy spectrum at the blade still includes a $\kappa^{-5/3}$ inertial subrange.

Airfoil cascade simulation

The evolution of the TKE and total pressure from the inlet of the blade domain along the middle passage and stagnation lines is shown in Figure 6. Although the Taylor and incompressibility hypotheses are questionable with the large TKE value injected at the inlet, the rapid TKE decay ensures a short transient upstream of the blade. In the middle passage of the blade, $(0 \leq x/c_{ax} \leq 1)$, $0.7k_{ref} \leq k \leq 0.85k_{ref}$, which is still close to the target experimental value and corresponds to an absolute difference in terms of turbulence intensity of 0.7%. As a side effect of the rapid TKE decay, a total pressure drop of about 1% is also observed close to the inlet and had to be compensated to target the same total pressure at the blade as in the experiments.

A visualisation of the flow highlighting the separation, the recirculation bubble, and the reattachment near the trailing edge of the blade is then presented in Figure 7, with line integral convolution (LIC) of the mean shear stress on the blade and the mean velocity field on the periodic plane. This visualisation of quantities represented by fourth-order polynomials on a second-order mesh was performed using a ParaView plugin developed by Rasquin et al. (2019).

Afterwards, the distribution of isentropic Mach number M_{is} over the critical region of the blade is shown in Figure 8, along with the total pressure loss profile in the wake of the blade. In both cases, a good agreement with experimental data is obtained, while RANS simulations typically suffer to predict the M_{is} distribution and total pressure loss in the wake, as illustrated by Fard Afshar et al. (2023). Not shown here, the outflow angle is also well predicted by these DNS simulations compared to the experiments.

Finally, the TKE and dissipation ϵ_s fields normalized by their respective maximum value in the close wake of the blade are presented in Figures 9a and 9b. These two fields are included in the advanced statistics database generated for the LPT blade and highlight the increase of TKE and dissipation in the turbulent region of the blade after the reattachment of the boundary layer and in the close wake. The residual budget of the TKE derived from Equation (7) and the residual budget of the dissipation in Equation (18) are presented in Figures 9c and 9d respectively.
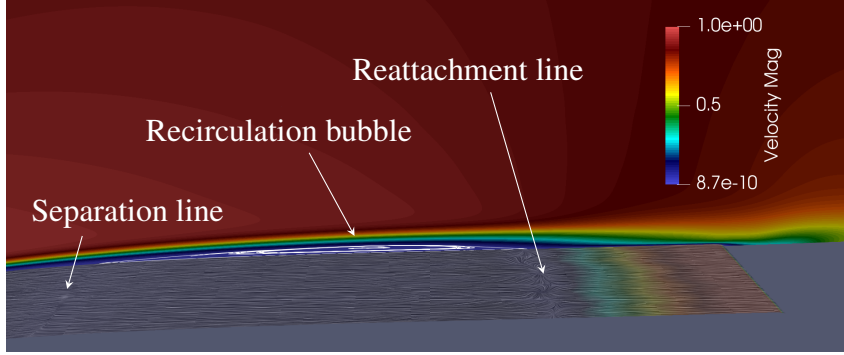
Figure 7: **Visualisation of the flow separation and reattachment near the trailing edge, with line integral convolution (LIC) of the mean shear stress on the blade and the mean velocity field on the periodic plane**
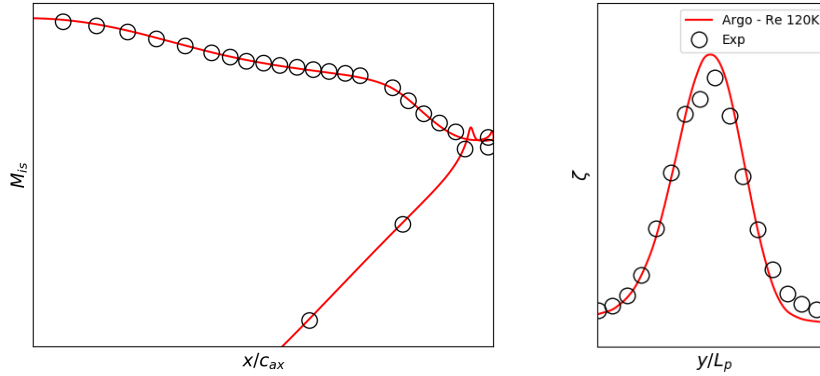

Figure 8: **Comparison of the isentropic Mach number M_{is} near the trailing edge (left) and total pressure loss ζ in the wake of the LPT blade (right) with experimental data**

Each residual is normalized by respectively the maximum value of the production term in Equation 9 and the viscous destruction term in Equation 26 located in the close wake of the blade. This normalization choice is based on the observation that these two terms provide the largest contribution in absolute value to the TKE and dissipation budget respectively in the close wake region. These residual budgets appear to be well close except in a few cells in the close wake of the blade where the normalized TKE residual budget rises to 20% of the production term and the normalized dissipation residual budget to 60% of the viscous destruction term, which is coherent with the mesh resolution shown in Figure 2

CONCLUSIONS

A workflow to generate high-fidelity databases for the improvement of turbulence models has been presented. This workflow relies on the compressible high-order DGM flow solver named Argo developed at Cenaero. A particular emphasis has been given to the injection of representative turbulence fluctuations at the inlet of the computational domain, which is based on a precursor simulation featuring a decay of homogeneous isotropic turbulence.

The target high-fidelity databases include all the terms required for the reconstruction of
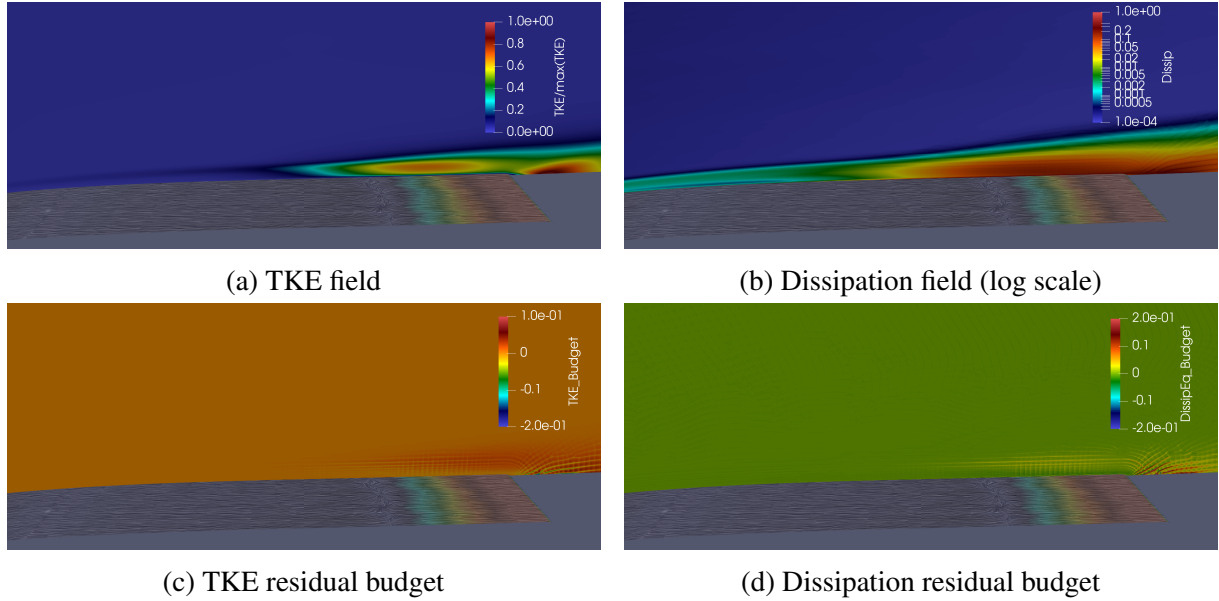
11

(a) TKE field

(b) Dissipation field (log scale)

(c) TKE residual budget

(d) Dissipation residual budget

Figure 9: **Normalized TKE and dissipation fields, along with their respective normalized residual budget near the trailing edge**

three equations useful for various families of RANS turbulence models: the Favre averaged Navier-Stokes, Reynolds stress (and therefore kinetic energy), and dissipation equations.

The turbulence injection procedure has been validated on a typical LPT airfoil cascade at $Re_{2th} = 120000$, $M_{2th} \approx 0.6$ and $p_{t1} \approx 16000$ Pa, with a good agreement of the M_{is} distribution on the blade and p_t loss in the wake. The next step of this work will consist in analyzing and exploiting these high-fidelity database for the improvement of RANS models applied to this LPT airfoil cascade.

References

Carton de Wiart, C., Hillewaert, K., Bricteux, L., and Winckelmans, G. (2015). Implicit les of free and wall-bounded turbulent flows based on the discontinuous galerkin/symmetric interior penalty method. *International Journal for Numerical Methods in Fluids*, 78(6):335–354.

Carton de Wiart, C., Hillewaert, K., Duponcheel, M., and Winckelmans, G. (2014). Assessment of a discontinuous galerkin method for the simulation of vortical flows at high reynolds number. *International Journal for Numerical Methods in Fluids*, 74(7):469–493.

Cockburn, B., Karniadakis, G. E., and Shu, C.-W. (2012). *Discontinuous Galerkin methods: theory, computation and applications*, volume 11. Springer Science & Business Media.

Cocle, R., Bricteux, L., and Winckelmans, G. (2009). Scale dependence and asymptotic very

high reynolds number spectral behavior of multiscale subgrid models. *Physics of Fluids*, 21(8):085101.

Dhamankar, N. S., Blaisdell, G. A., and Lyrintzis, A. S. (2018). Overview of turbulent inflow boundary conditions for large-eddy simulations. *Aiaa Journal*, 56(4):1317–1334.

Duraisamy, K., Iaccarino, G., and Xiao, H. (2019). Turbulence modeling in the age of data. *Annual review of fluid mechanics*, 51:357–377.

Fard Afshar, N., Kozulovic, D., Henninger, S., Deutsch, J., and Bechlars, P. (2023). Turbulence anisotropy analysis at the middle section of a highly loaded 3d linear turbine cascade using large eddy simulation. *Journal of the Global Power and Propulsion Society*, 7:71–84.

Gerolymos, G. and Vallet, I. (2001). Wall-Normal-Free Reynolds-Stress Closure for Three-Dimensional Compressible Separated Flows. *AIAA Journal*, 39(10):1833–1842.

Geuzaine, C. and Remacle, J.-F. (2009). Gmsh: A 3-d finite element mesh generator with built-in pre-and post-processing facilities. *International journal for numerical methods in engineering*, 79(11):1309–1331.

Hillewaert, K. and Rodi, W. (2022). List of desirable and minimum quantities to be entered into the KB Wiki. ERCOFTAC KB WIKI (`https://kbwiki-images.s3.amazonaws.com/8/80/List_of_desirable_and_minimum_quantities_to_be_entered_into_the_KB_Wiki.pdf`).

Hunt, J. and Savill, A. (2005). Guidelines and criteria for the use of turbulence models in complex flows. *Prediction of turbulent flows*, 340:291–343.

Keating, A. and Piomelli, U. (2006). A dynamic stochastic forcing method as a wall-layer model for large-eddy simulation. *Journal of Turbulence*, 7:N12.

Knight, D. D. (1997). Numerical simulation of compressible turbulent flows using the Reynolds-Averaged Navier-Stokes equations. In *AGARD FDP Special Course on "Turbulence in Compressible Flows"*, volume AGARD-R-819, von Karman Institute for Fluid Dynamics, Rhode-St-Genèse, Belgium. AGARD.

Kreuzinger, J., Friedrich, R., and Gatski, T. (2006). Compressibility effects in the solenoidal dissipation rate equation: A priori assessment and modeling. *International Journal of Heat and Fluid Flow*, 27:696–706.

Larsson, J. (2009). Blending technique for compressible inflow turbulence: Algorithm localization and accuracy assessment. *Journal of Computational Physics*, 228(4):933–937.

Menter, F. R., Kuntz, M., and Langtry, R. (2003). Ten years of industrial experience with the sst turbulence model. *Turbulence, heat and mass transfer*, 4(1):625–632.

Passot, T. and Pouquet, A. (1987). Numerical simulation of compressible homogeneous flows in the turbulent regime. *Journal of Fluid Mechanics*, 181:441–466.

Pope, S. B. (2000). *Turbulent flows*. Cambridge University Press.

Rasquin, M., Bauer, A., and Hillewaert, K. (2019). Scientific post hoc and in situ visualisation of high-order polynomial solutions from massively parallel simulations. *International Journal of Computational Fluid Dynamics*, 33(4):171–180.

Rogallo, R. S. (1981). Numerical experiments in homogeneous turbulence. Technical Memorandum NASA-TM-81315, NASA Ames.

Spalart, P. (2010). Reflections on rans modelling. In *Progress in hybrid RANS-LES modelling*, pages 7–24. Springer.

Vincent, P., Witherden, F., Vermeire, B., Park, J. S., and Iyer, A. (2016). Towards green aviation with python at petascale. In *SC'16: Proceedings of the International Conference for High Performance Computing, Networking, Storage and Analysis*, pages 1–11. IEEE.

Wilcox, D. C. et al. (1998). *Turbulence modeling for CFD*, volume 2. DCW industries La Canada, CA.

Wu, X. (2017). Inflow turbulence generation methods. *Annu. Rev. Fluid Mech*, 49(1):23–49.

Xiong, Z., Nagarajan, S., and Lele, S. K. (2004). Simple method for generating inflow turbulence. *AIAA Journal*, 42(10):2164–2166.